



Experimental investigation of in-flow fluidelastic instability for rotated triangular tube bundles subjected to single-phase and two-phase transverse flows

Philippe Piteau, Xavier Delaune, Domenico Panunzio, Romain Lagrange, Jose Antunes

► To cite this version:

Philippe Piteau, Xavier Delaune, Domenico Panunzio, Romain Lagrange, Jose Antunes. Experimental investigation of in-flow fluidelastic instability for rotated triangular tube bundles subjected to single-phase and two-phase transverse flows. *Journal of Fluids and Structures*, 2023, 123, pp.104005. 10.1016/j.jfluidstructs.2023.104005 . cea-04271749

HAL Id: cea-04271749

<https://cea.hal.science/cea-04271749>

Submitted on 20 Dec 2023

HAL is a multi-disciplinary open access archive for the deposit and dissemination of scientific research documents, whether they are published or not. The documents may come from teaching and research institutions in France or abroad, or from public or private research centers.

L'archive ouverte pluridisciplinaire **HAL**, est destinée au dépôt et à la diffusion de documents scientifiques de niveau recherche, publiés ou non, émanant des établissements d'enseignement et de recherche français ou étrangers, des laboratoires publics ou privés.

EXPERIMENTAL INVESTIGATION OF IN-FLOW FLUIDELASTIC INSTABILITY FOR ROTATED TRIANGULAR TUBE BUNDLES SUBJECTED TO SINGLE-PHASE AND TWO-PHASE TRANSVERSE FLOWS*

Philippe Piteau¹⁺, Xavier Delaune¹, Domenico Panunzio¹, Romain Lagrange¹, Jose Antunes²

¹ *Université Paris-Saclay, CEA, Service d'Études Mécaniques et Thermiques,
F-91191, Gif-sur-Yvette, France*

² *Centro de Ciências e Tecnologias Nucleares (C2TN), IST, Universidade de Lisboa,
2695-066 Bobadela LRS, Portugal*

ABSTRACT

The in-flow fluidelastic instability of tube bundles prompted renewed interest since the recent unanticipated failure of the replacement steam generators at the San Onofre nuclear power station. A literature review on the topic discloses contrasting views, depending on the tube bundle and flow configuration addressed. In a recent paper, the authors reported experiments using square bundles, subjected to single and two-phase flows. No streamwise instability was observed, for the tested bundle configurations and the flow velocity ranges explored. In the present paper, experimental results obtained at CEA-Saclay for a rotated triangular tube bundle are presented, providing new in-flow fluidelastic data for both single-phase and two-phase transverse flows. The bundle consists of 50 tubes, with reduced pitch $P/D=1.44$ and tube diameter $D=30\text{mm}$. It was subjected to single-phase (air or water) and two-phase air-water (with homogeneous void fraction in the range 40% to 98%) transverse flows. In the upper region of the bundle, several different flexibility configurations were tested, with up to 15 flexible tubes, mounted using anisotropic supports, which allow for in-flow vibrations. Results presented in the paper include in-flow fluidelastic stability data obtained for both single-phase and two-phase transverse flows. A detailed modal identification of the bundle under natural turbulence excitation was performed, at several flow velocities, highlighting the modeshapes which are prone to in-flow instability. Moreover, local void fraction and identified flow regimes are also presented. These results are discussed and compared to those obtained by previous authors, for similar tested configurations.

1. Introduction

In-flow fluidelastic instability of tube bundles (e.g., involving tube motions along the drag/streamwise direction) has been the subject of a strong renewed interest, since the unanticipated failure of the replacement steam generators of the San Onofre Nuclear Generating Station (SONGS) in 2012 - see the report from SCE (2012) and the documents referred therein. In-flow fluidelastic instability occurred in the U-bend region of the tube bundle, where the anti-vibration bars were ineffective to prevent instabilities of the low-frequency in-plane U-bend tube modes. Note that, in this upper region of the bundle, tubes are essentially excited by a two-phase ascending secondary cross-flow, with high values of the void fraction.

Before this event, in-flow fluidelastic instability was usually considered irrelevant, although early studies by Weaver and Koroyannakis (1983) and Weaver and Schneider (1983) had reported the possibility of streamwise instability, depending on features of the flow and the tested bundles. Their findings were further explored and refined about 20 years later, through experiments in air flow performed by Mureithi et al. (2005) and in two-phase flow performed by Janzen et al. (2005) and Violette et al. (2006). Then, the SONGS failure triggered an enlarging corpus of recent experimental and theoretical work, aiming clarification of the issues posed by test results. Delaune's (2016) review of the experimental literature on the topic, involving references up to 2015, discloses contrasting views, which may be broadly condensed as follows:

* This paper is an expanded version of the paper presented at the 12th International Conference on Fluid-Induced Vibration, July 5-8, 2022, Paris-Saclay, France.

+ Corresponding author: philippe.piteau@cea.fr

For *square bundles* fitted with asymmetrically supported tubes, in-flow fluidelastic instability was never observed under single-phase flows. On the other hand, symmetrically supported tubes lead to fluidelastic coupling forces that induce time-varying planar and/or orbitally coupled motions, from which it is problematic to assert a dominant instability configuration. To the authors' best knowledge, experimental in-flow response data from square bundles is virtually nonexistent for two-phase flows. In a recent paper, Delaune et al. (2018) reported experiments under single and two-phase flows. No streamwise instability was observed, for the tested bundle configurations and the flow velocity ranges explored.

For *triangular bundles*, in-flow fluidelastic instability was observed under single-phase flows, the stability boundary being dependent on the number of flexible tubes, while for two-phase flows in-flow instability does not seem to depend consistently on the bundle flexibility configuration. However, for a single flexible tube within a rigid bundle, no in-flow instability was ever observed, whatever the nature of the flow. In any case, for both single-phase and two-phase flows, the in-flow instability boundary is always beyond the cross-flow instability boundary.

References published since 2015 provided new experimental data on the in-flow fluidelastic instability of triangular bundles. The work by Feenstra et al. (2017) concerns U-bend tube regions in a rotated triangular configuration (with $P/D=1.5$) subjected to air cross-flow, with gap-controlled flat bar supports. Their results show in-plane fluidelastic instability, which may need a manual pushing help to trigger. They also observed a significant delay before the bundle instability emerged, these findings denoting that the in-plane fluidelastic coupling is quite weak. Nakamura and Tsujita (2018) tested three straight bundles, in a rotated triangular configuration (with $P/D=1.2\sim 1.5$), also subjected to air flow. They obtained stream-wise instability with Connors' constant values in the range $K = 7.5 \sim 10$, higher than typically observed for transverse instability. Tan et al. (2018) tested straight bundles, in a rotated triangular configuration (with $P/D=1.48$), subjected to single phase water flow and two-phase air-water flow. The tubes were supported by rectangular flexible bars, allowing to test fluidelastic instability along either the lift or the drag direction. According to the authors, their tests did not produce in-flow instabilities.

The work performed by Azuma et al. (2018) is part of a significant effort performed by Mitsubishi Heavy Industries related to stream-wise instabilities. In a very comprehensive experimental program, these authors tested triangular straight and U-bend tube bundles (with $P/D=1.33$) subjected to a SF₆-Ethanol mixture, which displays near-similar density and surface tension to air-steam two-phase flow. Experiments were performed for several flexible tube configurations, flow distributions and void fractions. The Connors instability constant was identified for both the out-of-plane and in-plane motions. For in-flow instabilities, a significant dispersion of K was obtained, ranging from the order of magnitude for out-of-plane instability up to 5 times larger, depending on the bundle type (straight or U-bend) and on the tube modal frequencies. The lower values of K pertain to the straight tube bundles with higher modal frequencies. Also from this research group, the recent paper by Nishida et al. (2021) reports extensive measurements of the unsteady fluidelastic coupling forces in triangular straight and U-bend tube bundles (with $P/D=1.33$) subjected to actual steam-water flows under high temperature and pressure, which is a rare achievement. Results are presented for both cross-flow and in-flow instabilities. They then inserted the identified flow-coupling coefficients into the general Chen (1983) formulation and computed instability boundaries that compared favorably with the experimental critical velocities. Surprisingly, from their study, for isotopic mounted straight tubes, in-flow instability will arise at a lower velocity than the cross-flow instability. For U-tube bundles, the in-line critical velocities were found to be higher.

The present paper follows our preceding investigation documenting the absence of in-flow instability for square bundles, see Delaune et al. (2018). Here we present the results of an extensive experimental investigation, performed at CEA-Saclay, on the streamwise stability features of a rotated

triangular bundle, providing new in-flow fluidelastic data for both single-phase and two-phase transverse flows. The bundle consists essentially on 10 rows of 5 tubes, with reduced pitch $P/D=1.44$ and tube diameter $D=30\text{mm}$. It was subjected to single-phase (air or water) and two-phase air-water transverse flows. Several different flexibility configurations were tested, with up to 15 flexible tubes, mounted using anisotropic supports, which allow for in-flow vibrations. Results presented include streamwise fluidelastic stability data obtained for both single-phase and two-phase flows. Also, a detailed modal identification of the bundle under natural turbulence excitation was performed using the NExT-ERA technique, see for instance Kordkheili et al. (2018), and compared with the computed fluid-coupled bundle modes under stagnant fluid conditions, using the finite element CEA-program CAST3M. These results highlight the modeshapes which are prone to in-flow fluidelastic instability. Moreover, local void fraction and identified flow regimes are also presented. These results are discussed and compared to those obtained by previous authors, for similar tested configurations.

2. Experimental rig

The tests were performed using the experimental rig TITAN (Fig. 1) with the CEA-Saclay air/water loop GASCOGNE (Fig. 2). As shown, the rotated triangular bundle consists of 50 tubes (10 rows, 5 columns) with reduced pitch $P/D=1.44$, tube diameter $D=30\text{mm}$ and length $L=300\text{mm}$, completed by two rows of half-tubes attached to the test-section walls. The rigid lower 20 tubes of the bundle are used to condition the incoming vertical flow, before the test section.

For the tested bundle configurations, as illustrated in Fig. 3 for configuration C1 with 15 vibrating tubes, each flexible tube is supported through a flexible rectangular bar with $100\times 25\times 4\text{mm}$, positioned such that maximum flexibility is along the streamwise direction. All the flexible tubes display nearly identical values for the first modal frequency and damping values in air. For motions along the in-flow (drag) direction, the relevant average and standard deviation values are given in Table 1. For each tested configuration, tubes with the first streamwise bending modal frequency at 32Hz and 14Hz (in air) were tested. The lower modal frequency was obtained by adding an extra mass at the end of the flexible tubes, so that fluidelastic instabilities were eventually reached at lower flow velocities. The second streamwise and the first transverse flexural modal frequencies were measured one order of magnitude higher than the frequency range of interest.



Fig. 1. Test rig TITAN of CEA-Saclay.

Concerning the flow, Fig. 2 (left side) shows a general view of the test loop. Water flow is provided by a centrifugal pump, delivering up to 1080 m³/h, while air is supplied by a compressor with a maximal flow of 3000 m³/h (at 0°C and 1 Bar). As shown in the figure, the two fluids are mixed prior to the test section where the tube bundle is located. Tests were performed for single-phase (air, water) and two-phase air-water flows at various void fractions.

Concerning the instrumentation, as shown in Fig. 2 (right side, upper drawing), each flexible tube is equipped with a strain gauge, located near the clamped side, calibrated with respect to the tube displacement at the free end. On the other hand, Fig. 2 (right side, lower drawing) shows the lateral opening for inserting the sapphire bioptical probe, which was located between the 3rd and 4th rows of the bundle, in order to measure the local void fraction of two-phase flows.

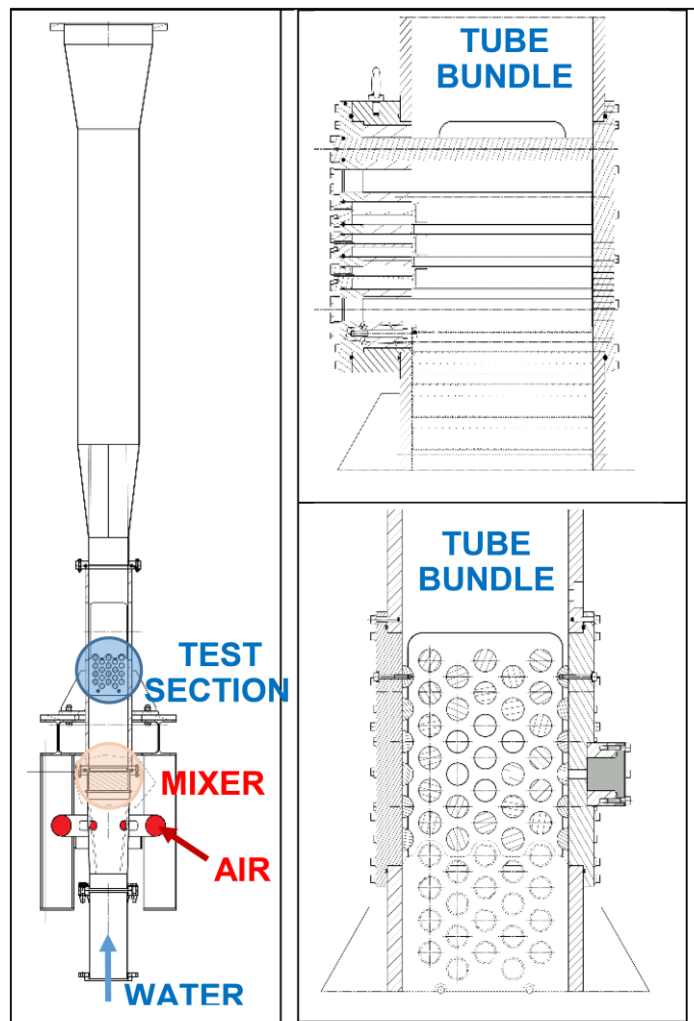


Fig. 2. Air/water experimental loop GASCOGNE of CEA-Saclay.

	Tubes « 32Hz »		Tubes « 14Hz »	
	Frequency	Damping	Frequency	Damping
Average	31.96Hz	0.047%	14.18Hz	0.045%
Dispersion	0.84%	21.9%	0.66%	7.6%

Table 1. Average values and RMS dispersion of the flexible tubes first streamwise modal frequencies and damping values, for the two tested modal frequencies in air.

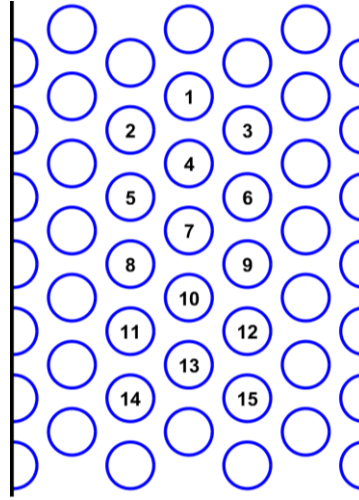


Fig. 3. Configuration C1 with 15 in-flow flexibly supported tubes.

3. Experimental procedures

The first tests were performed, for the different flexible configurations, with the higher frequency "32Hz" tubes, for single-phase (air, water) and two-phase flows (with homogeneous void-fraction 40, 80, 90, 95 and 98%). Then, in order to reach streamwise fluidelastic instability, a significant number of tests was also performed using the lower frequency flexible "14Hz" tubes.

In all cases, the flow rate was increased until the mean tube drag plus the peak vibration amplitude nearly reached the gap between tubes (0.013m). Figure 4 shows the measured mean drag of the tubes when the water velocity is increased, for configuration 1 (see Fig. 3). As might expected, the drag increases in quadratic manner with the flow pitch velocity V_p .

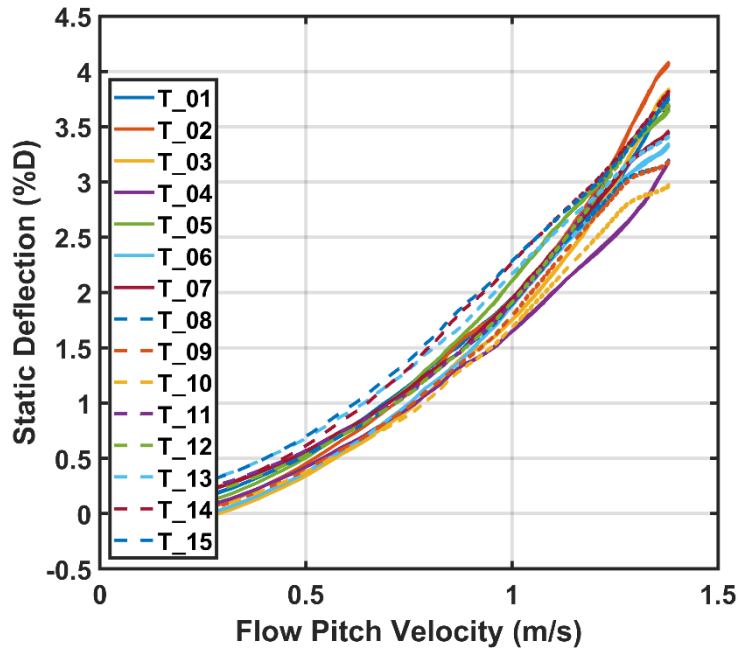


Fig. 4. Static drag of the in-flow flexible tubes as a function of the flow pitch velocity.

Beyond these preliminary static drag drift tests and the standard statistics of the tubes vibration amplitudes and spectral content, as a function of the flow velocity, a specific feature of the present experiments is that a full modal identification of the vibrating tube bundle was performed from the in-line turbulence responses of all the flexibly mounted tubes, as a function of the flow gap-velocity. For such a purpose, the identification method NExT-ERA (Natural Excitation Technique - Eigensystem Realization Algorithm) technique, developed by Juang & Pappa (1985) and further developed by several authors, see James (1993). This identification method in the time-domain, based on a state-space representation of the dynamical system and on concepts originated from control theory, proved efficient enough for the purposes of the present work. The ERA identification method can be implemented in polyreference, and thus enable identification of modes with near-identical frequencies.

In its time-discrete state-space form, the system state dynamics are written at time t_k as:

$$\mathbf{y}(t_k) = \mathbf{A}\mathbf{y}(t_{k-1}) + \mathbf{B}\mathbf{u}(t_{k-1}) \quad , \quad \mathbf{y}(t_k) \equiv \begin{Bmatrix} \mathbf{x}(t_k) \\ \dot{\mathbf{x}}(t_k) \end{Bmatrix} \quad (1)$$

where $\mathbf{u}(t_k)$ is the excitation vector and $\mathbf{y}(t_k)$ the response vector, while the output vector $\mathbf{z}(t_k)$ is:

$$\mathbf{z}(t_k) = \mathbf{C}\mathbf{y}(t_k) \quad (2)$$

and matrices \mathbf{A} , \mathbf{B} and \mathbf{C} stand for the time-discrete state-space matrix model. Assuming impulse excitations $\mathbf{u}(t_0) = \delta(t_0)$, one obtains from (1)-(2) the recurrence for the ensemble $\mathbf{Z}(t_k)$ of all system responses at r locations to all system excitations at e locations:

$$\mathbf{Z}(t_k) = \mathbf{C}\mathbf{A}^{k-1}\mathbf{B} \quad (3)$$

with matrices \mathbf{A} , \mathbf{B} and \mathbf{C} yet unknown.

At this step, from the ensemble of impulse responses $\mathbf{Z}(t_k)$, one can build a Hankel matrix $\mathbf{H}(t_k)$ as usual, with a given number s of time-samples per column and a number d of delayed columns, both numbers large enough to encompass the maximum rank of the Hankel matrix:

$$\mathbf{H}(t_k) = \begin{bmatrix} \mathbf{Z}(t_{k+1}) & \mathbf{Z}(t_{k+2}) & \mathbf{L} & \mathbf{Z}(t_{k+d}) \\ \mathbf{Z}(t_{k+2}) & \mathbf{Z}(t_{k+3}) & \mathbf{L} & \mathbf{Z}(t_{k+d+1}) \\ \mathbf{M} & \mathbf{M} & \mathbf{O} & \mathbf{M} \\ \mathbf{Z}(t_{k+s}) & \mathbf{Z}(t_{k+s+1}) & \mathbf{L} & \mathbf{Z}(t_{k+s+d-1}) \end{bmatrix} \quad (4)$$

which can be written as the matrix product:

$$\mathbf{H}(t_k) = \mathbf{P}_s \mathbf{A}^k \mathbf{Q}_d \quad (5)$$

where \mathbf{P}_s and \mathbf{Q}_d are the observability and controllability matrices, respectively, see Juang & Pappa (1985). The SVD decomposition of the Hankel matrix of order zero leads to:

$$\mathbf{H}(t_0) \equiv \mathbf{H}_0 = \mathbf{P}_s \mathbf{A}^0 \mathbf{Q}_d = \mathbf{P}_s \mathbf{Q}_d = \mathbf{U} \mathbf{\Sigma} \mathbf{V}^T \Rightarrow \begin{cases} \mathbf{P}_s = \mathbf{U} \mathbf{\Sigma}^{1/2} \\ \mathbf{Q}_d = \mathbf{\Sigma}^{1/2} \mathbf{V}^T \end{cases} \quad (6)$$

hence, the Hankel matrix of order one reads:

$$\mathbf{H}(t_1) \equiv \mathbf{H}_1 = \mathbf{P}_s \mathbf{A}^1 \mathbf{Q}_d = \mathbf{U} \mathbf{\Sigma}^{1/2} \mathbf{A} \mathbf{\Sigma}^{1/2} \mathbf{V}^T \quad (7)$$

and a suitable truncation order m is chosen, in order to filter noise and other non-physical artefacts, in order to obtain a minimal model realization:

$$\mathbf{U} = \begin{bmatrix} \mathbf{U}_m \\ \mathbf{0} \end{bmatrix} ; \quad \mathbf{\Sigma} = \begin{bmatrix} \mathbf{\Sigma}_m & \mathbf{0} \\ \mathbf{0} & \mathbf{0} \end{bmatrix} ; \quad \mathbf{V} = \begin{bmatrix} \mathbf{V}_m \\ \mathbf{0} \end{bmatrix} \quad (8)$$

so that, from (7) and (8), one obtains a minimal estimation of the dynamical matrix \mathbf{A} :

$$\mathbf{A} = \mathbf{\Sigma}_m^{-1/2} \mathbf{U}_m^T \mathbf{H}_1 \mathbf{V}_m \mathbf{\Sigma}_m^{-1/2} \quad (9)$$

while the other minimal state matrices are obtained as discussed by Juang & Pappa (1985):

$$\mathbf{B} = \mathbf{\Sigma}_m^{1/2} \mathbf{V}_m^T \mathbf{E}_e \quad ; \quad \mathbf{C} = \mathbf{E}_m^T \mathbf{U}_m \mathbf{\Sigma}_r^{1/2} \quad (10)$$

where \mathbf{E}_r and \mathbf{E}_e are the r^{th} order and e^{th} order selector matrices. Matrix \mathbf{A} contains the essentials of the state dynamics, through the eigen-formulation:

$$\mathbf{A} \hat{\boldsymbol{\phi}}_n = \hat{\boldsymbol{\phi}}_n \hat{\lambda}_n \quad , \quad n = 1, 2, L, m \quad (11)$$

Then, the system modal frequencies ω_n and damping values ζ_n are extracted from the eigenvalues of (11), after conversion to the corresponding continuous state-space model:

$$\lambda_n = \frac{\ln(\hat{\lambda}_n)}{\Delta t} = -\omega_n \zeta_n \pm i \omega_n \sqrt{1 - \zeta_n^2} \quad , \quad n = 1, 2, L, m \quad (12)$$

and, similarly, the system modeshapes $\boldsymbol{\phi}_n$ are obtained from the eigenvectors $\hat{\boldsymbol{\phi}}_n$ of the discrete formulation as:

$$\boldsymbol{\phi}_n = \mathbf{C} \hat{\boldsymbol{\phi}}_n \quad , \quad n = 1, 2, L, m \quad (13)$$

In its basic form, the ERA method deals with the modal identification from the free responses of systems subjected to impulse excitations. For those subjected to wideband random excitations $\mathbf{u}(t)$, such as unmeasured aerodynamic loads, the NExT development by James (1993) replaces the use of the forced random system responses $\mathbf{X}(t)$ by their cross-correlation functions $\mathbf{R}_{\mathbf{X}\mathbf{X}_R}(t)$, where $\mathbf{X}_R(t_k)$ stands for reference responses. These correlations and their derivatives also comply with the system dynamical equations, so that:

$$\mathbf{M} \ddot{\mathbf{X}}(t) + \mathbf{D} \dot{\mathbf{X}}(t) + \mathbf{K} \mathbf{X}(t) = \mathbf{F}_e(t) \quad (14)$$

is equivalent to:

$$\mathbf{M} \ddot{\mathbf{R}}_{\mathbf{X}\mathbf{X}_R}(\tau) + \mathbf{D} \dot{\mathbf{R}}_{\mathbf{X}\mathbf{X}_R}(\tau) + \mathbf{K} \mathbf{R}_{\mathbf{X}\mathbf{X}_R}(\tau) = \mathbf{R}_{\mathbf{F}_e \mathbf{X}_R}(\tau) \quad (15)$$

and, as the assumed random excitation is uncorrelated with the responses, $\mathbf{R}_{\mathbf{F}_e \mathbf{X}_R}(\tau) \approx \mathbf{0}$. The original forced problem (14) is then replaced by the equivalent free response formulation:

$$\mathbf{M} \ddot{\mathbf{R}}_{\mathbf{X}\mathbf{X}_R}(\tau) + \mathbf{D} \dot{\mathbf{R}}_{\mathbf{X}\mathbf{X}_R}(\tau) + \mathbf{K} \mathbf{R}_{\mathbf{X}\mathbf{X}_R}(\tau) = \mathbf{0} \quad (16)$$

which encapsulates the same modes as (14) and can be identified by the ERA method. When the NExT-ERA technique is used for system identification under unmeasured excitations, it is obviously not possible to identify the state-matrix \mathbf{B} from formulation (16). This is of no consequence, as the system modal features are extracted from matrices \mathbf{A} and \mathbf{C} , see equations (11)-(13).

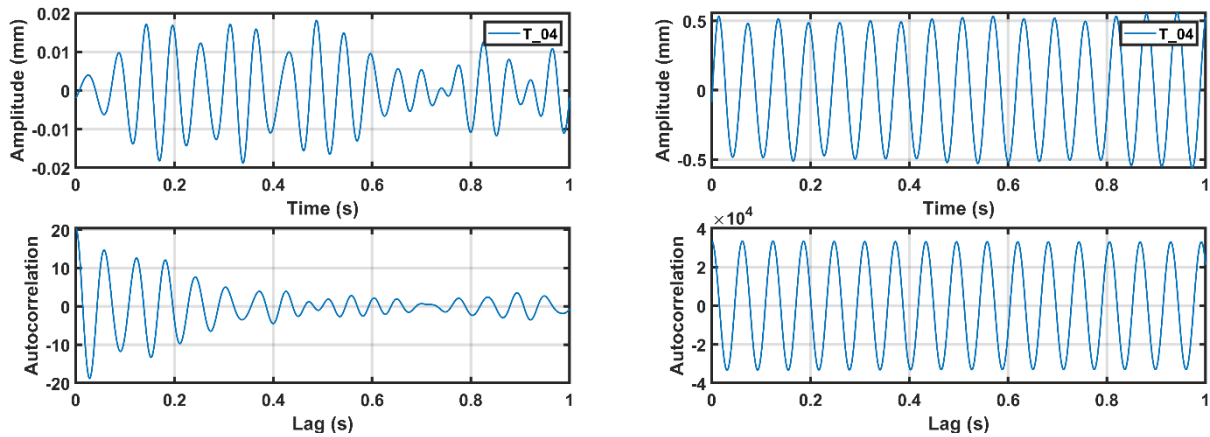


Fig. 5. Motion response and autocorrelation of the tube 4: $U_p = 0.481$ m/s (left); $U_p = 0.724$ m/s (right).

Figure 5 (left upper side) illustrates a typical random response of tube 4, under steady conditions at flow pitch velocity 0.481 m/s, lower that the flutter instability boundary, as well as the corresponding autocorrelation function in Figure 5 (left lower side). These plots illustrate well how the correlation function reproduces the tube free response and damping behavior. Figure 5 (right upper side) shows the results obtained at flow pitch velocity 0.724 m/s, higher that the flutter instability boundary, as well as the corresponding autocorrelation function in Figure 5 (right lower side). These results pertain to the limit cycles of the linearly unstable tube, hence the near-similarity of the motion amplitude and of the correlation function.

In Fig. 6 (left side) we illustrate the confidently identified modes using the NExT-ERA method, from the 15 tube responses at pitch velocity 0.481 m/s, under stable conditions. Theoretically, 15 modes stem from this flexible configuration, but several tools have been used to highlight those identifications deserving most confidence, not only from several "Mode Indicators", see Pappa & Elliott (1993), but also from the modeshape orthogonality, as illustrated in Fig. 6 (right side). In the following one will notice that, as the flow velocity increases, so does the quality of the modeshape orthogonality diagram.

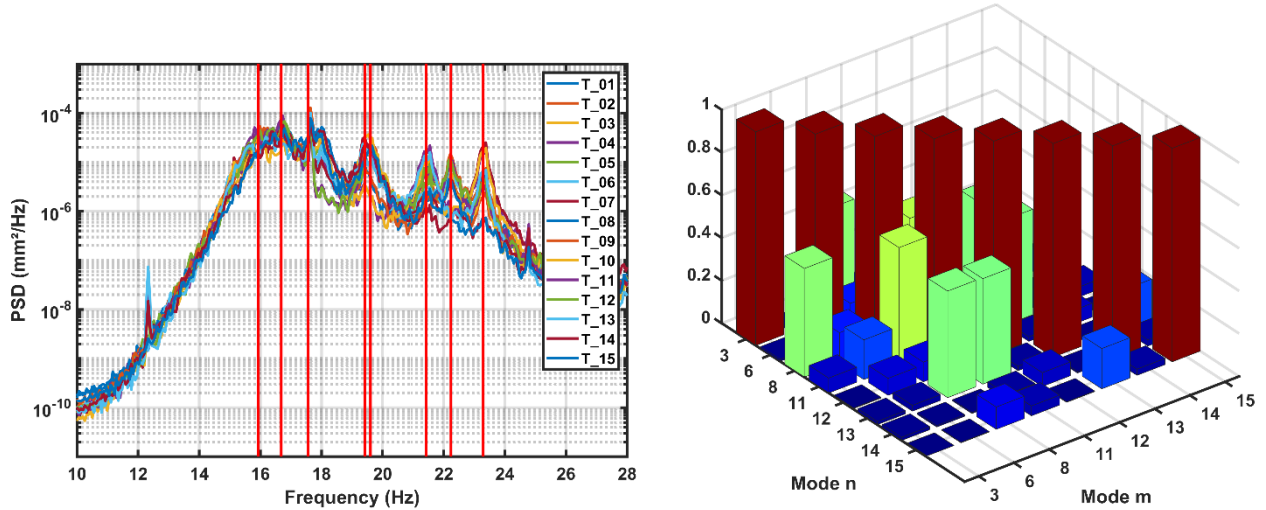


Fig. 6. Bundle immersed in water flow at pitch velocity $U_p = 0.481$ m/s : Confidently identified flow-coupled modes, at the frequencies of the red lines (left); Orthogonality diagram of the identified modes (right).

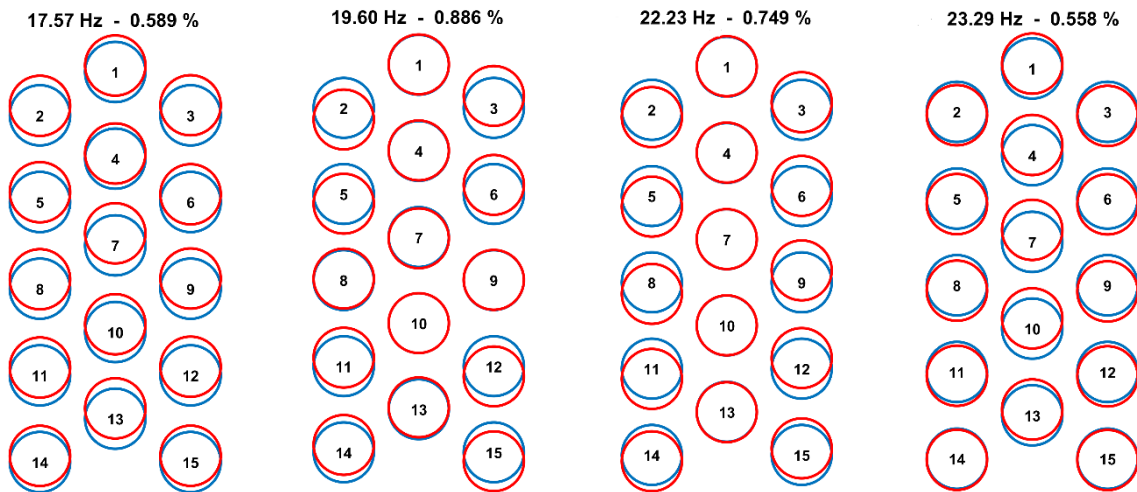


Fig. 7. Illustrative identified modes of the bundle immersed in water flow at pitch velocity $U_p = 0.481$ m/s .

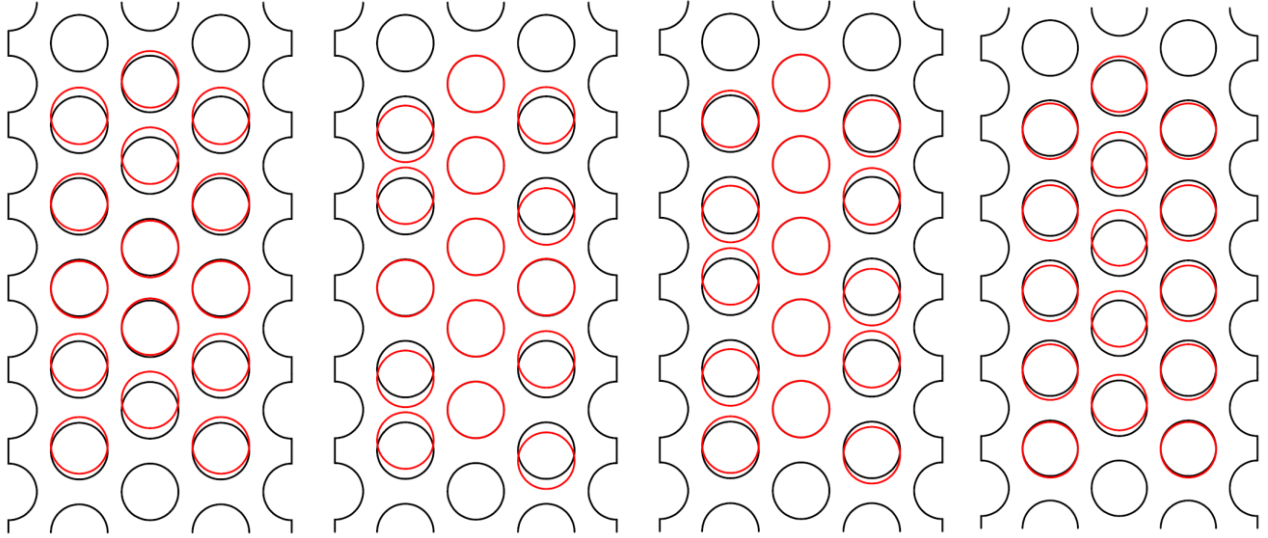


Fig. 8. Fluid mesh and illustrative computed modes of the bundle immersed in stagnant water and coupled by the fluid, using program CAST3M.

In Fig. 7 we illustrate some examples of the experimentally identified bundle collective modeshapes, pertaining to the results shown in Fig. 6 (left side), at pitch velocity 0.481 m/s. These illustrative modal plots clearly show definite symmetrical and anti-symmetrical tube motion patterns. Figure 8 shows the corresponding modes, computed under stagnant fluid conditions, using the finite element program CAST3M, developed at CEA-Saclay. There are some obvious differences in details, not only because the computational model has no imperfections, geometrical or mechanical, which is obviously not the case of the experimental rig. Even so, the similitude of the identified and computed bundle modes is obvious, giving confidence on both procedures and results. Notice that, most often, there are entire tube columns which not vibrate, or nearly so, strongly suggesting that cross-coupling between tube columns is of second order importance, as far as in-flow instability is concerned.

4. Single-phase flow experiments

Figure 9 presents the experimental results obtained for configuration C1, using the higher frequency 15 flexible tubes ("32Hz") subjected to air flow, for increasing pitch velocity. The left plot shows the experimental streamwise response spectra of the central tube 7 (see Fig. 3), while the right plot displays the RMS response amplitudes of all the flexible tubes. Figure 10 presents the results obtained for configuration C1 in air flow, when using the lower frequency flexible tubes ("14Hz"). Both figures clearly highlight an instability of the modal response peak, which arises at about 17 m/s for the "32Hz" tubes and about 13 m/s for the "14Hz" tubes.

Figures 11 and 12 present the corresponding test results, when configuration C1 is subjected to water flow. Not only the modal frequencies are lowered, due to the water added mass effect, but one can also notice that the single modal peaks displayed by the air tests are now replaced by groups of modal peaks spanning a significant frequency range, due to a strong tube coupling by the denser fluid.

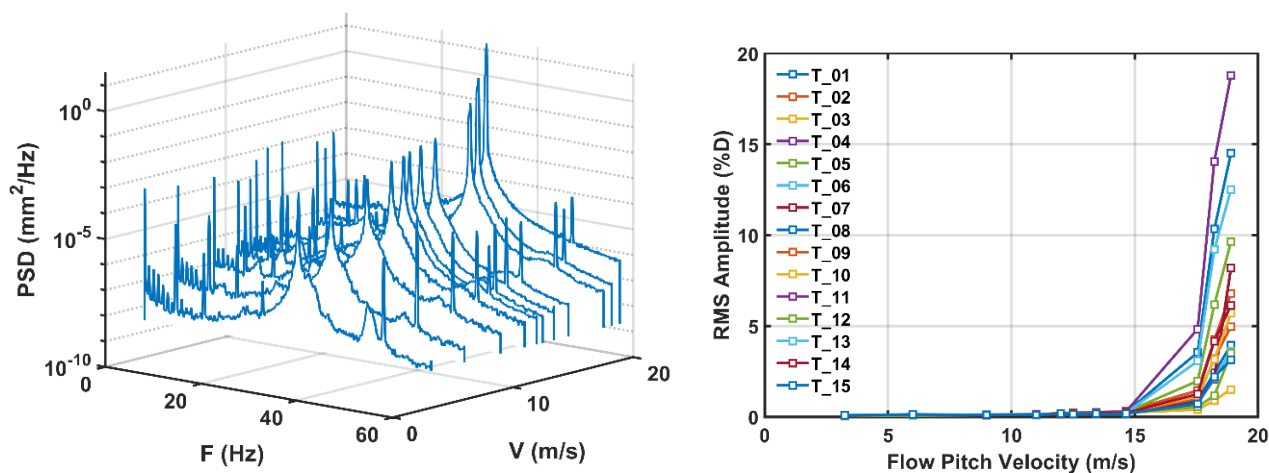


Fig. 9. Configuration C1 "32Hz" in air flow: Response spectra of tube 7 and RMS amplitudes of all the flexible tubes as a function of the pitch velocity.

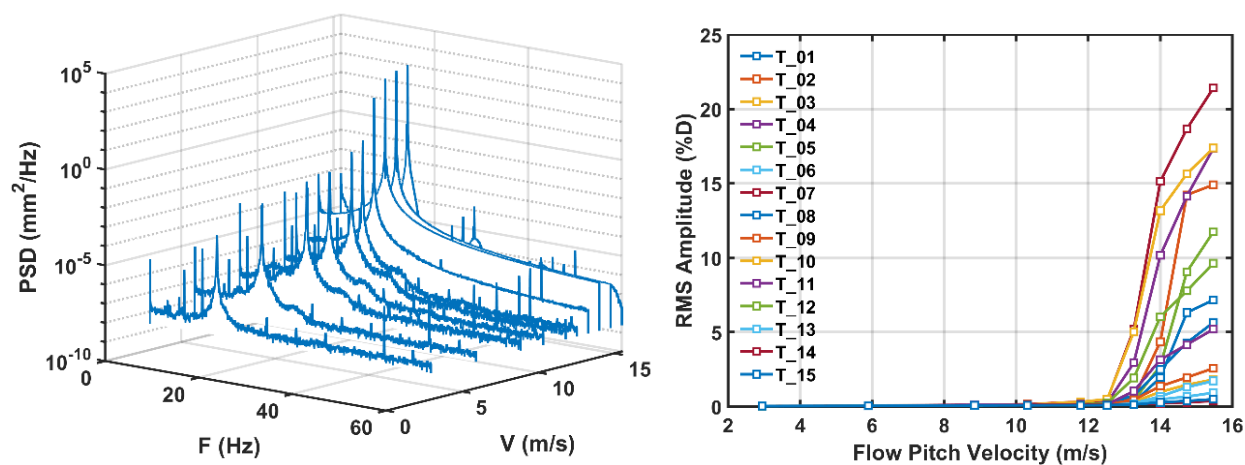


Fig. 10. Configuration C1 "14Hz" in air flow: Response spectra of tube 7 and RMS amplitudes of all the flexible tubes as a function of the pitch velocity.

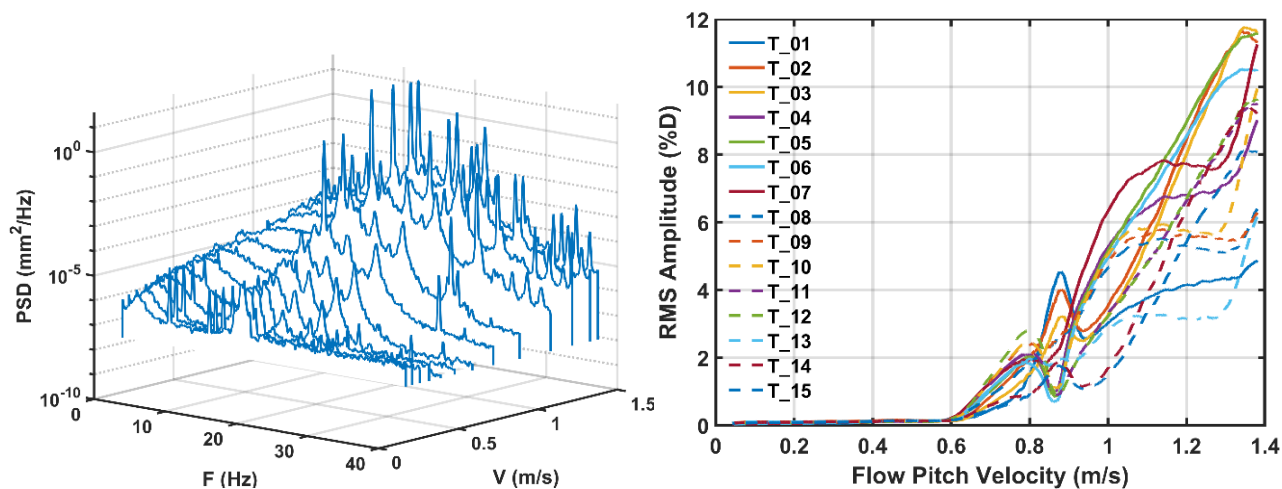


Fig. 11. Configuration C1 "32Hz" in water flow: Response spectra of tube 7 and RMS amplitudes of all the flexible tubes as a function of the pitch velocity.

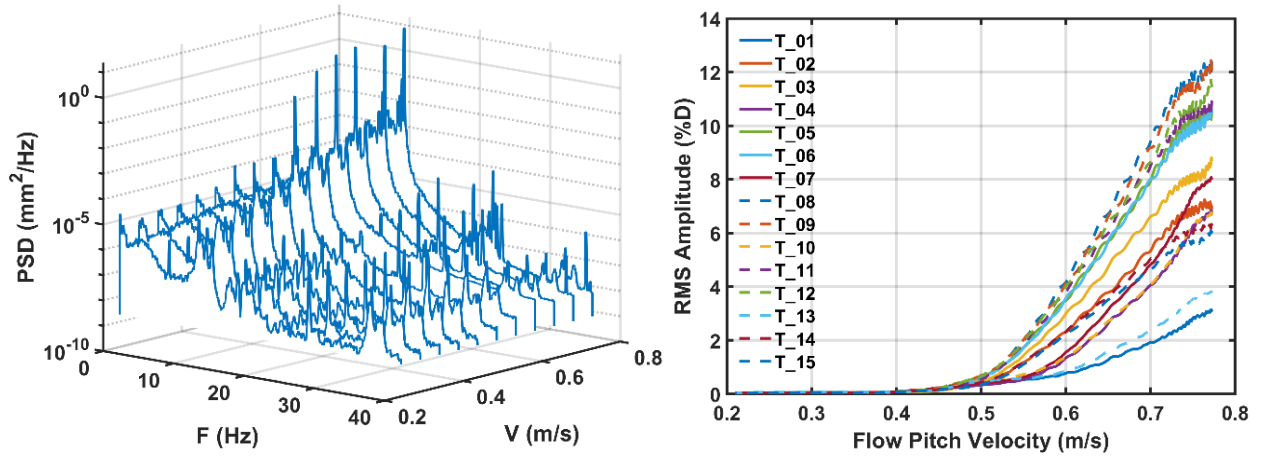


Fig. 12. Configuration C1 "14Hz" in water flow: Response spectra of tube 7 and RMS amplitudes of all the flexible tubes as a function of the pitch velocity.

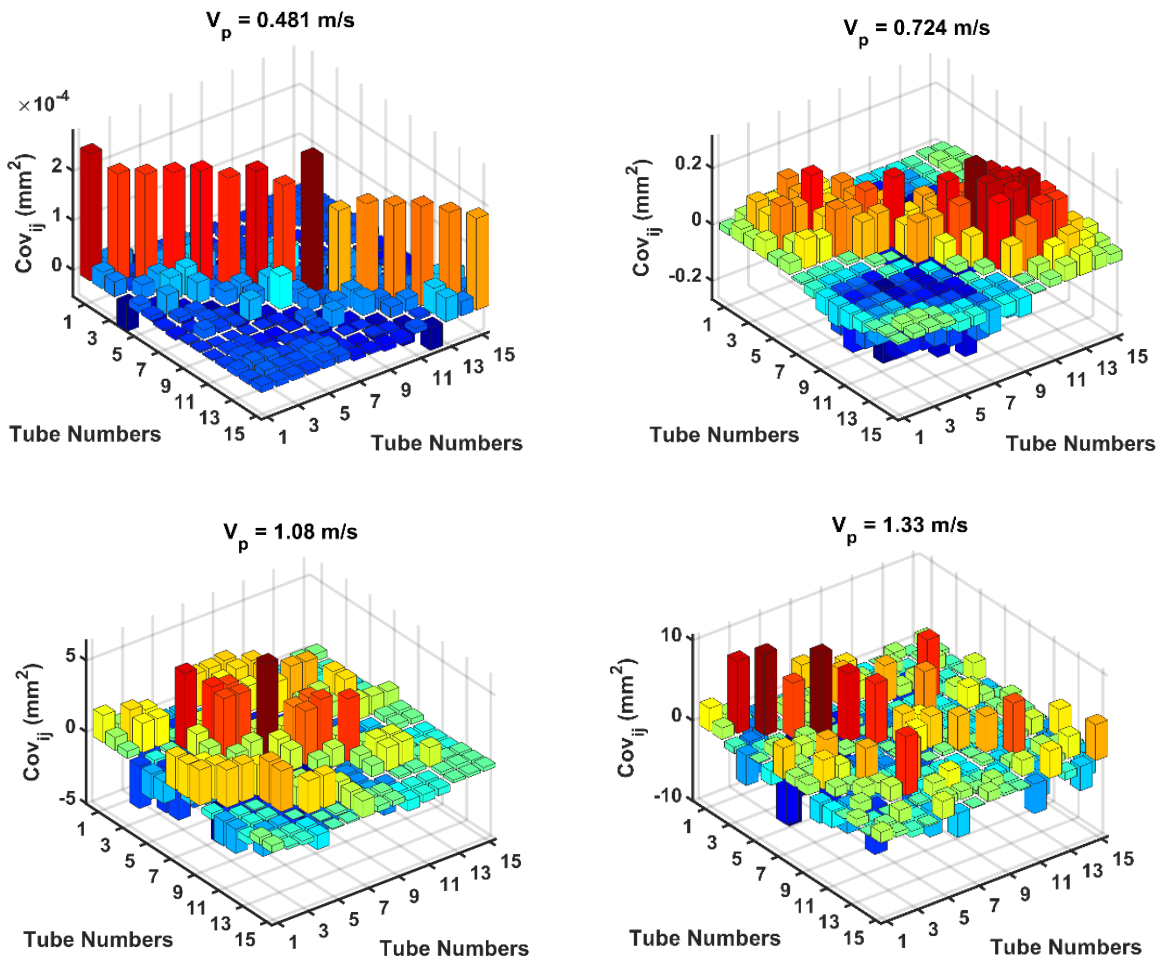


Fig. 13. Configuration C1 "32Hz" in water flow: Covariance matrix of the 15 vibrating tubes for three increasing values of the flow pitch velocity.

For the "32Hz" tubes in water, the modal group ranges from 16 to 24Hz, while for the "14Hz" tubes in water, the modal group ranges from 11 to 13Hz. The experimental data in water flow displays unstable behavior beyond about 0.6 m/s for the "32Hz" tubes and about 0.4 m/s for the "14Hz" tubes. The slope of the increasing amplitude responses, beyond the instability boundary, is much steeper for the tests in air flow than for those in water flow.

The results shown in Fig. 11 are particularly interesting. One can notice in the lower plot that the lines displaying the tube RMS amplitudes are interlaced, so that the tube with maximum response amplitude changes with the flow velocity. The upper plot shows that this behavior is due to switching of the unstable mode as the flow velocity increases.

The covariance matrices shown in Fig. 13, computed from the measured time-domain responses of the flexible tubes at increasing flow velocities, further confirm that the bundle response pattern changes significantly as the flow velocity increases. At 0.481 m/s, below the critical velocity (0.6 m/s), the covariance matrix is nearly diagonal, so that tube motions are uncorrelated. Beyond the critical stability boundary, the covariance matrices at flow pitch velocities 0.724 m/s, 1.08 m/s and 1.33 m/s point to specific motion cross-correlations, although with changing patterns. Such interesting behavior is possibly related to the fluidelastic forces changes with the reduced velocity, and to the forces projections on the different bundle modes.

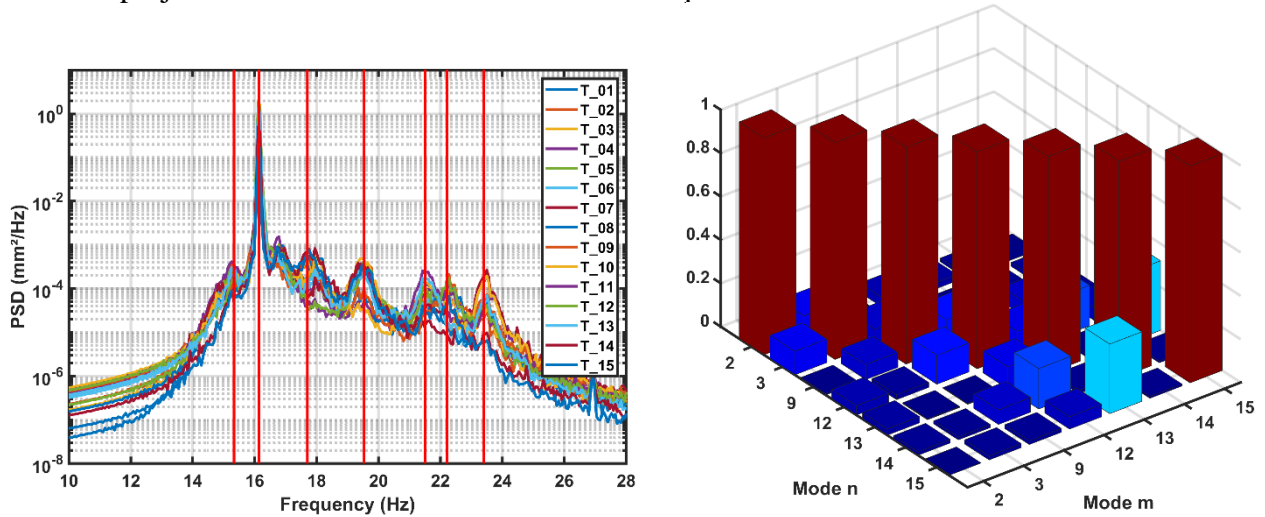


Fig. 14. Bundle immersed in water flow at pitch velocity $U_p = 0.724$ m/s : Confidently identified flow-coupled modes, at the frequencies of the red lines (left); Orthogonality diagram of the identified modes (right).

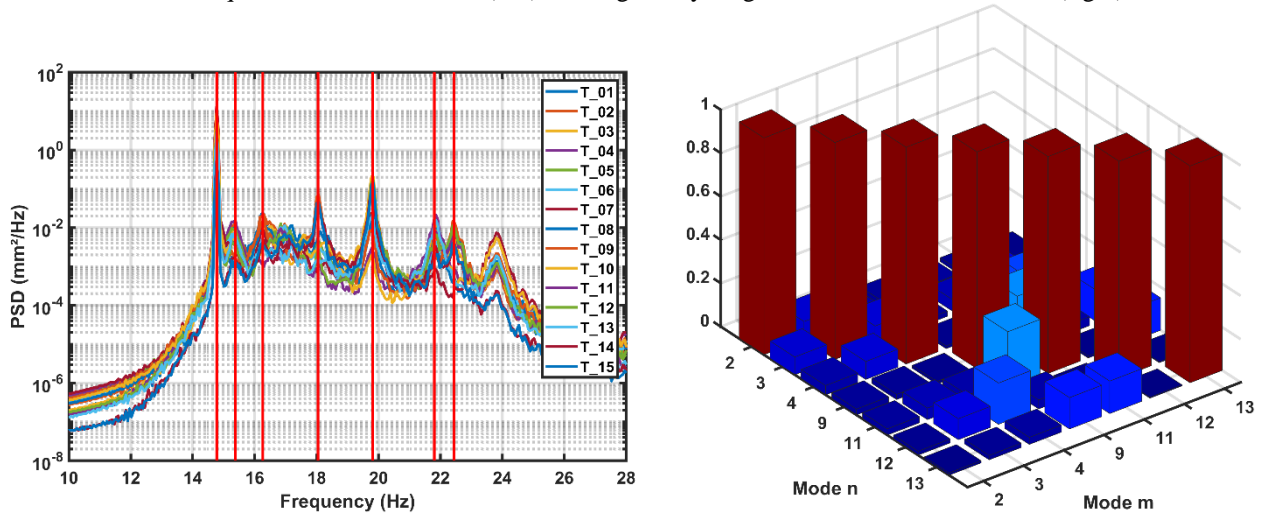


Fig. 15. Bundle immersed in water flow at pitch velocity $U_p = 1.08$ m/s : Confidently identified flow-coupled modes, at the frequencies of the red lines (left); Orthogonality diagram of the identified modes (right).

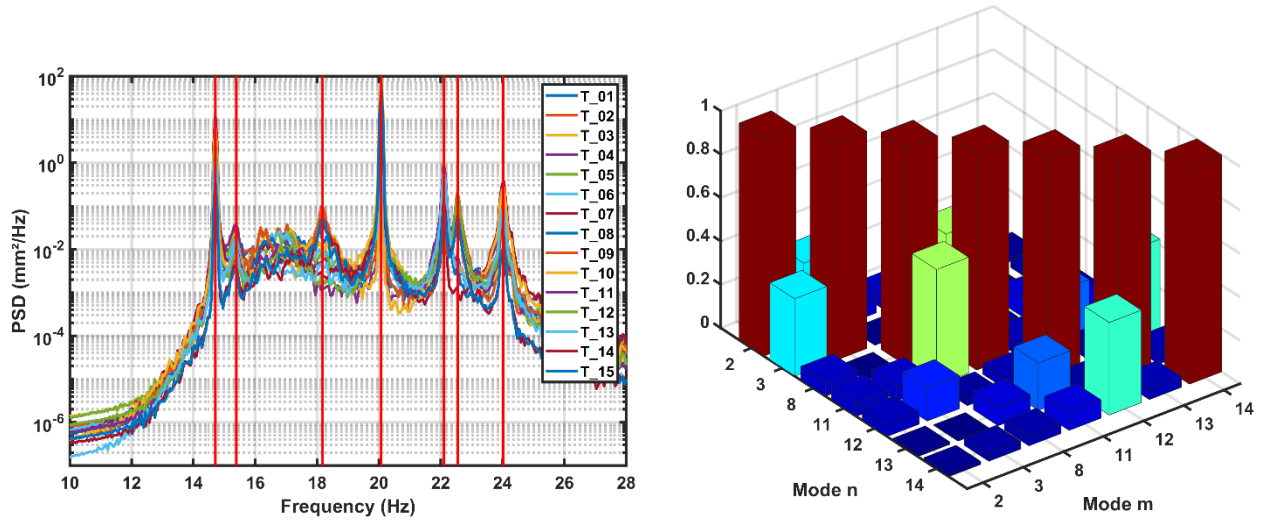


Fig. 16. Bundle immersed in water flow at pitch velocity $U_p = 1.33$ m/s : Confidently identified flow-coupled modes, at the frequencies of the red lines (left); Orthogonality diagram of the identified modes (right).

These findings can be better put in perspective by looking at the experimentally identified unstable modes, as a function of the flow pitch velocity. Firstly, the results presented in Figs. 14 to 16 show the response spectra of the 15 tubes and the corresponding confidently identified modes (at the frequencies of the red lines), as well as the orthogonality diagram of the identified modes, respectively for the flow pitch velocities of 0.724 m/s, 1.08 m/s and 1.33 m/s. These results show already that the confidently identified modes are in general quite orthogonal, hence that the identifications are reliable. Then, see Fig. 14, notice that at flow velocity 0.724 m/s the only unstable mode is near 16.2 Hz, the corresponding modeshape being shown in Fig. 17(a). However, at flow velocities 1.08 m/s and 1.33 m/s, in spite of a few spectral differences, there are mainly two unstable modes near 14.7 Hz and about 20 Hz, the corresponding modeshapes being shown in Fig. 17 (b-c). Notice that, the system being linearly unstable, the unstable modes vibrate nonlinearly through limit cycles, with a net damping value approaching zero. Therefore, the identified "modal damping" under such circumstances is only a residual artefact, with no relation whatsoever with the negative modal damping under linear unstable conditions. Overall, the results obtained in Figs. 14 to 17 are consistent with the global RMS amplitudes shown in Fig. 11 and support our results interpretation.

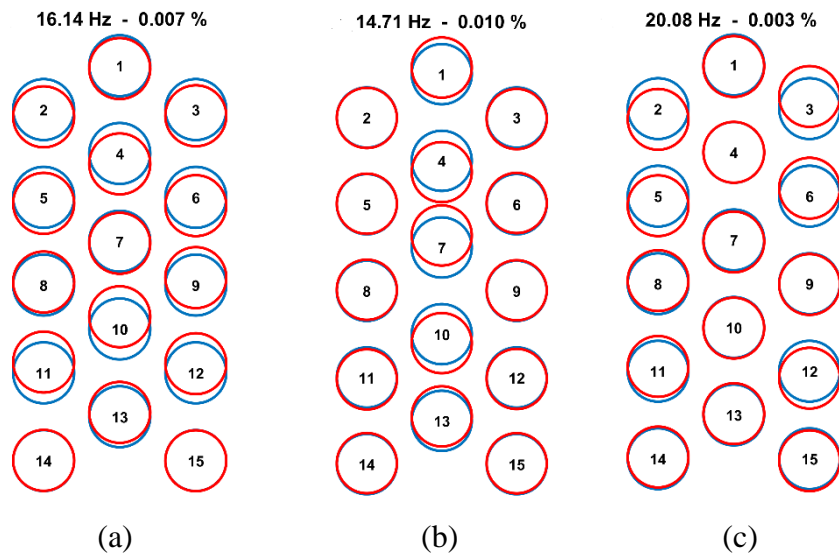


Fig. 17. Modeshapes of the unstable modes: (a) Pitch velocity 0.724 m/s; (b-c) Pitch velocities 1.08 m/s and 1.33 m/s.

Additional single-phase flow tests were performed for other flexible tube arrangements, as discussed in section 6.

5. Two-phase flow experiments

Figures 18 to 21 summarize the experimental results obtained for the flexible configuration C1, subjected to air-water flows. Figures 18 and 19 concern the higher frequency "32Hz" tubes, while Figs. 20 and 21 relate to the lower frequency "14Hz" tubes. Results are illustrated for two void fractions, 40% (Figs. 18 and 20) and 80% (Figs. 19 and 21). For both void fractions, the higher frequency tubes did not reach instability, in the range of homogeneous velocity explored, see Figs. 18 and 19.

Such is not the case for the lower frequency tubes, which display instabilities at about 3.8 m/s (40% void fraction) and 5.3 m/s (80% void fraction), see Figs. 20 and 21. One might conjecture that, for a high enough flow rate, instability would be reached for the "32Hz" subjected to two-phase flow. However, as pointed earlier, this could not be attempted, as the maximum velocities explored in Figs. 18 and 19 already led to a tube drag plus random response that nearly reached the inter-tube gap.

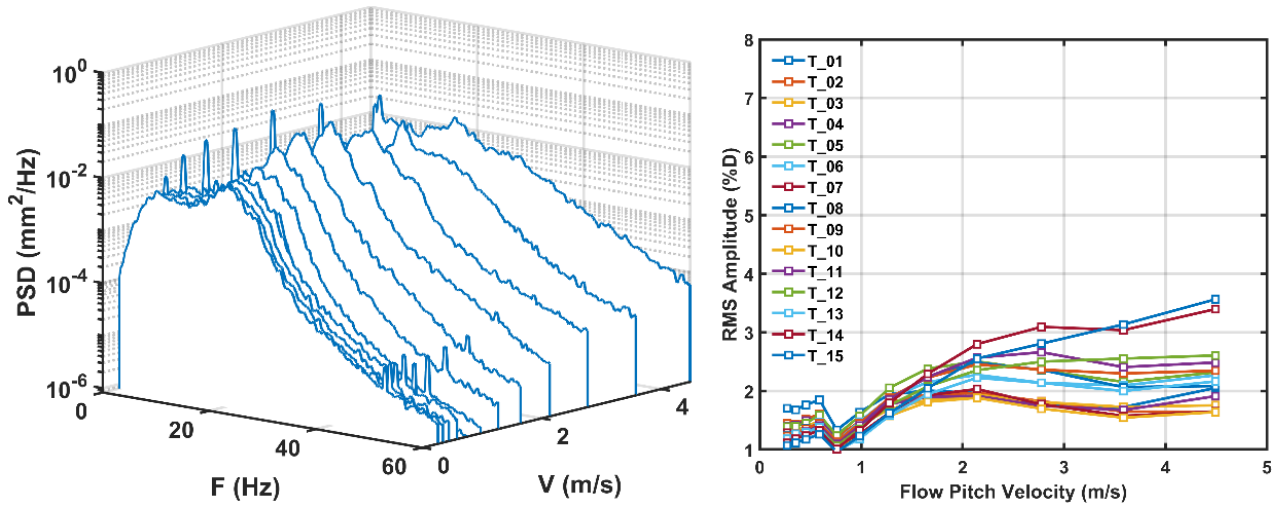


Fig. 18. Configuration C1 "32Hz" in air-water two-phase flow (void fraction 40%): Response spectra of tube 7 and RMS amplitudes of all the flexible tubes as a function of the pitch velocity.

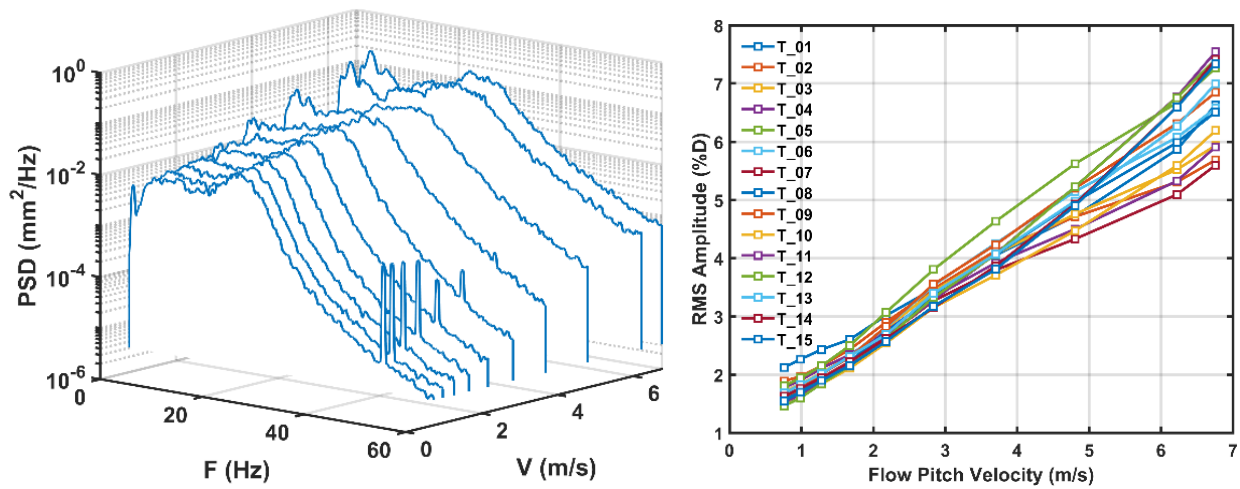


Fig. 19. Configuration C1 "32Hz" in air-water two-phase flow (void fraction 80%): Response spectra of tube 7 and RMS amplitudes of all the flexible tubes as a function of the pitch velocity.

An interesting feature in Fig. 18 is the non-monotone behavior of the RMS tube responses, as the flow velocity increases. It is suspected that this behavior is possibly connected with changes of the two-phase flow regime. Such an interpretation seems supported by the data presented in Fig. 22, which shows a two-phase flow chart experimentally obtained from the CEA air-water tests of a square bundle with $P/D=1.5$ (chart expanded from Delaune et al., 2018). The flow velocity region covered by the tests of Fig. 18, at 40% void fraction, is highlighted in Fig. 22, showing that the Bubbly and Slug flow regimes are intermixed.

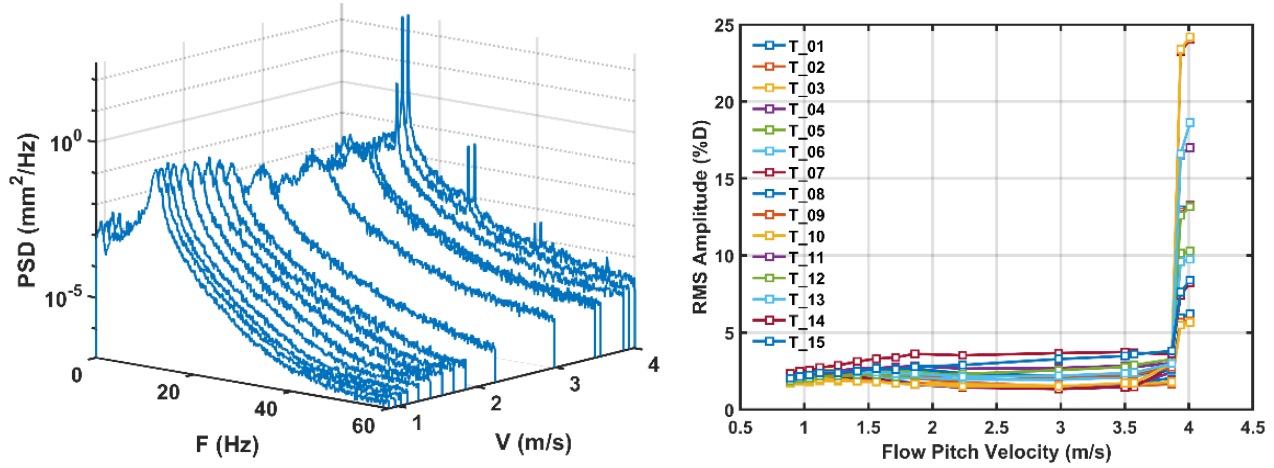


Fig. 20. Configuration C1 "14Hz" in air-water two-phase flow (void fraction 40%): Response spectra of tube 7 and RMS amplitudes of all the flexible tubes as a function of the pitch velocity.

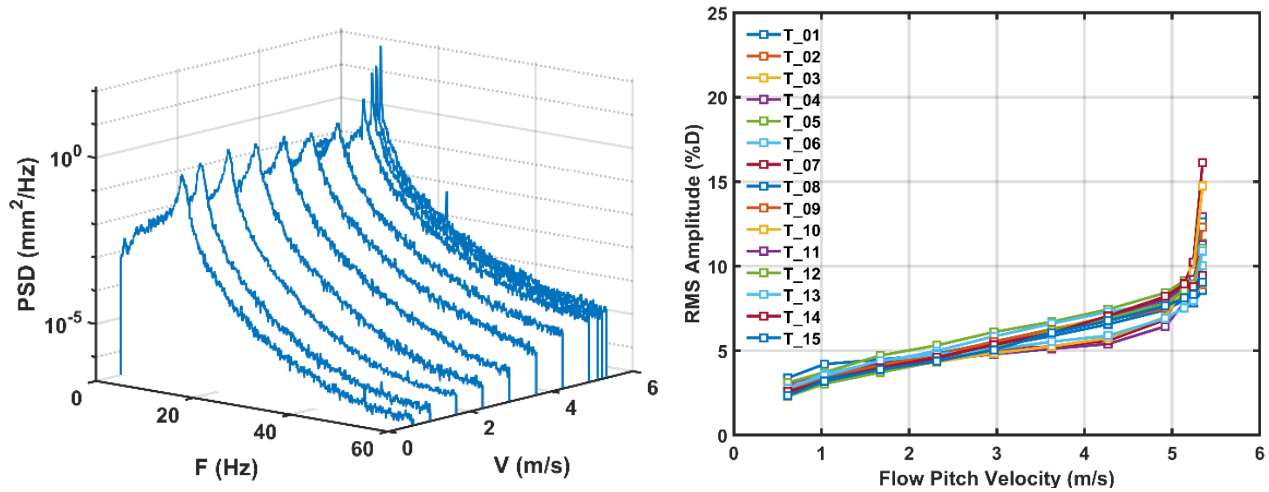


Fig. 21. Configuration C1 "14Hz" in air-water two-phase flow (void fraction 80%): Response spectra of tube 7 and RMS amplitudes of all the flexible tubes as a function of the pitch velocity.

Tests at other void fractions did not trigger instability for the "32Hz" tubes, while it was clearly reached for the "14Hz" tubes. This is the very reason why the lower frequency tubes were tested. Actually, because of their different mass and frequency parameters, our results from the "32Hz" tubes were ill-fitted for comparison with the instability data from Violette et al. (2006).

If one excepts the peculiar behavior shown in Fig. 18, most of our two-phase experiments led to a near-linear increase of the RMS tube amplitudes with the flow velocity, prior to instability. On the other hand, as can be seen in Figs. 18 and 19, a wideband low-frequency response often arises in the response spectra. This is a somewhat classical feature, often observed in vibration experiments using two-phase flows.

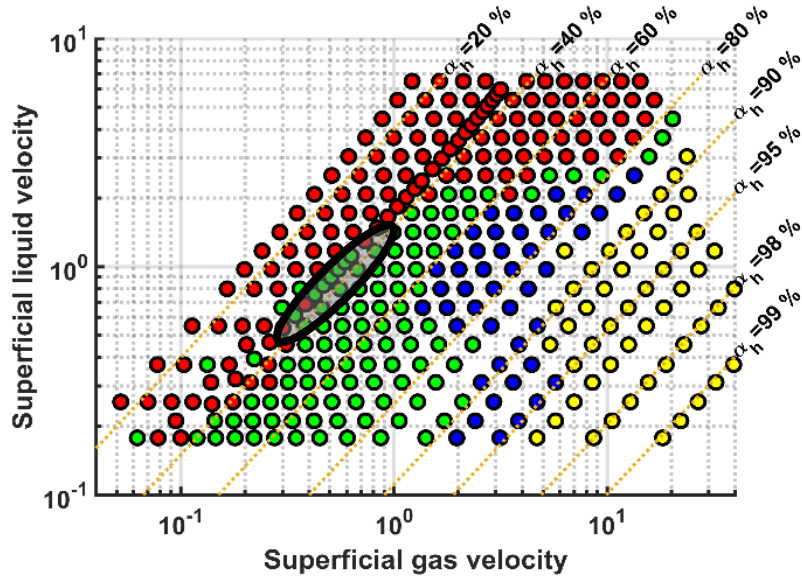


Fig. 22. Two-phase flow chart experimentally obtained from the CEA air-water tests of a square bundle with $P/D=1.5$ (expanded from Delaune et al., 2018); Flow regimes: Red=Bubbly, Green=Slug, Blue=Churn, Yellow=Annular.

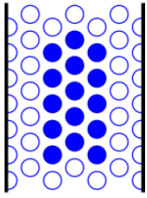
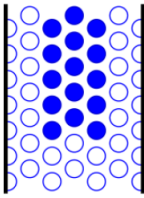
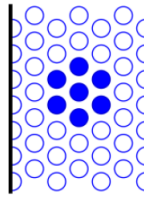
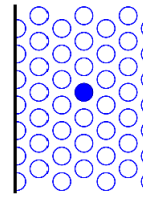
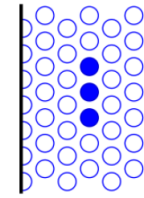
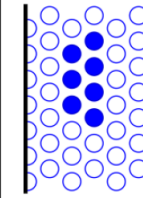
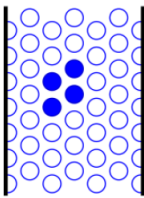
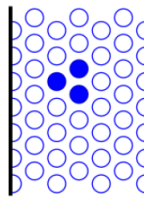
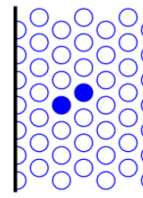
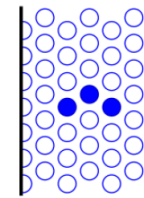
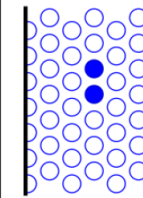
As for single-phase flows, additional two-phase flow tests were performed for configurations with various flexible tube arrangements. These experiments are described in the next section.

6. Other tested configurations

Figure 23 shows the many flexible configurations that were tested, most of them for the lower frequency "14Hz" tubes, to which the results of Fig. 23 apply (except for configuration C3, which was only tested with the "32Hz" tubes). Configuration C2 is also a 15 flexible tube arrangement, just as the "centered" configuration C1, but displaced towards the bundle end. Configuration C3 is a centered seven-tube cell. Configuration C4 is a single flexible tube at the center of the bundle. Then, configurations C5 to C11 explore different arrangements, using three to seven flexible tubes.

Figure 23 synthetizes the occurrence or not of streamwise fluidelastic instability for each configuration, under air flow, water flow and two-phase flow. Results of configuration C2 are similar to those of C1, with unstable behavior under single-phase and two-phase flows. The cell C3 (with "32Hz" tubes) became unstable under single-phase flow, but not for two-phase flow. The single flexible tube C4 never went unstable, in agreement with experiments by Violette et al. (2006). Concerning the other configurations, one can notice that those with a single flexible tube per column (C9 and C10) never became unstable, whatever the flow type. All the other configurations, having two or more flexible tubes in one or two columns became unstable under air flow, but remained stable under water flow and two-phase flow.

All these results suggest that: (1) Streamwise instability occurs through the vibration coupling of two or more tubes along the bundle columns; (2) Coupling between tubes along the bundle rows is irrelevant for streamwise instability; (3) The destabilizing coupling forces are comparatively weak, so that instability may or not be triggered, depending on a number of factors such as the system damping.

										C1	
										Air	Yes
										Water	Yes
										2-Phase	Yes
											
C2		C3 (·)		C4		C5		C6			
Air	Yes	Air	Yes	Air	No	Air	Yes	Air	Yes		
Water	Yes	Water	Yes	Water	No	Water	No	Water	No		
2-Phase	Yes	2-Phase	No	2-Phase	No	2-Phase	No	2-Phase	No		
											
C7		C8		C9		C10		C11			
Air	Yes	Air	Yes	Air	No	Air	No	Air	Yes		
Water	No	Water	No	Water	No	Water	No	Water	No		
2-Phase	No	2-Phase	No	2-Phase	No	2-Phase	No	2-Phase	No		
											

(*) Results for configuration C3 with "32Hz" tubes, as this configuration was not tested with the "14Hz" tubes.

Fig. 23. Tested configurations with various arrangements of the "14Hz" flexible tubes; also shown is the occurrence (Yes) or not (No) of streamwise fluidelastic instability for each configuration, respectively under air flow, water flow and two-phase flow.

7. Summary of results

After the previous qualitative remarks on the features that seem to govern streamwise instability phenomena, we now summarize the instability data stemming from our experiments. Figure 24 displays the Connors stability map for the various tested configurations, under single-phase and two-phase flow:

$$\frac{U_p^{crit}}{fD} = K \sqrt{\frac{2\pi\zeta m}{\rho D^2}} \quad (17)$$

The values of the mass-damping parameter, as well as those of the critical reduced velocity are based on the numerical data collected in Table 2, for both the "32Hz" and "14Hz" tubes, the various tested flexible configurations, under single-phase and two-phase flows. The present results are also compared with those obtained by Violette et al. (2006).

Tubes « 32 Hz »							Tubes « 14 Hz »						
α (%)	U_p^{crit} (m / s)	m (kg / m)	$\frac{m}{\rho D^2}$	f (Hz)	ξ (%)	K	α (%)	U_p^{crit} (m / s)	m (kg / m)	$\frac{m}{\rho D^2}$	f (Hz)	ξ (%)	K
0	0.6	1.38	1.53	15.87	0.16	10.18	0	0.46	3.23	4.17	11.22	0.06	10.78
40	> 4.5	1.02	1.88	22.00	3	> 11.5	40	3.87	2.85	5.71	12.38	3.35	9.50
60	> 5.5	0.83	2.32	24.26	3	> 11.4	60	4.23	2.67	7.99	12.81	4.70	7.17
80	> 6.8	0.66	3.62	27.39	3	> 10.0	80	5.24	2.48	15.8	12.86	2.76	8.21
90	> 10	.57	6.21	29.50	3	> 10.4	90	7.00	2.39	29.3	13.31	2.54	8.10
95	> 15	0.52	11.30	30.75	3	> 11.2	95	9.84	2.34	54.9	13.68	1.84	9.52
98	20.5	0.49	25.87	31.58	3	> 9.8	98	13.7	2.31	130.1	13.81	1.20	10.57
99	-	-	-	-	-	-	99	16.3	2.30	236.2	14.10	0.297	18.35 ^(*)
100	17.5	0.48	444.4	31.84	.17	8.48	100	13.0	2.29	2120	14.37	0.057	10.94

(*) This could be a biased identification of K, due to the difficulty of controlling and monitoring a void ratio of 99%.

Table 2. Bundle configuration C1 - Tubes "32Hz" and "14Hz": Flow physical parameters and structural modal frequency and damping values, as well as the experimental streamwise Connors constant K, for increasing values of the two-phase void fraction.

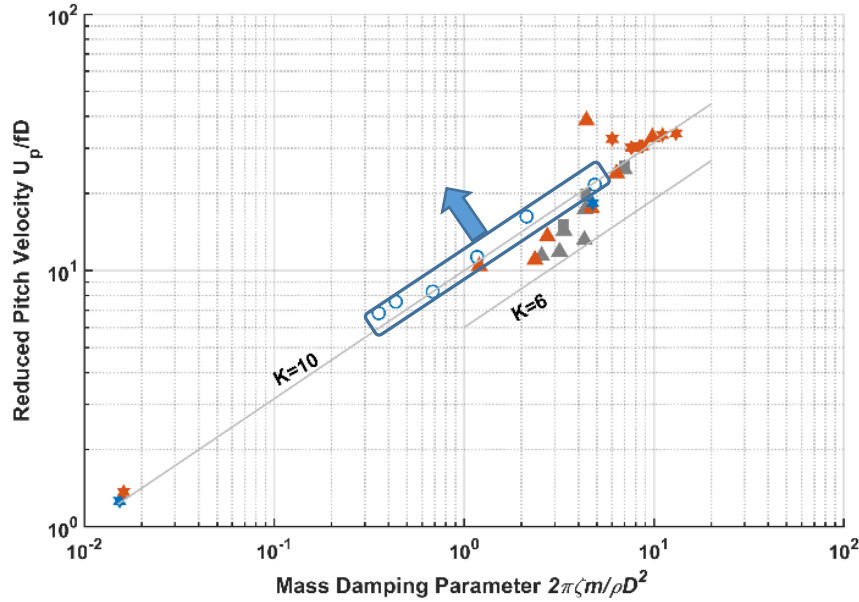


Fig. 24. Connors stability map from the test results: ○ Two-phase flow configuration C1 with "32Hz" tubes; ★ Single-phase flow configuration C1 with "32Hz" tubes; ▲ Two-phase flow configuration C1 with "14Hz" tubes; ★ Single phase flow configurations C1, C2, C5, C6, C7; C8, C11 with "14Hz" tubes; ■▲ Violette et al. (2006).

Concerning the damping values, in single-phase we use those measured for the most prominent mode at low flow velocity, while in two-phase flow this could only be achieved for the "14Hz" tubes. Due to identification difficulties, for the "32Hz" tubes in two-phase flow the maximum recommended value by ASME code $\zeta = 3\%$ was assumed.

Figure 24 shows that all the single-phase test results of configuration C1, for both the "32Hz" and "14Hz" tubes, in air flow and water flow, lay about the boundary stability line at $K = 10$. A similar result was obtained for the other tested configurations using "14Hz" tubes which became unstable in air flow. Concerning two-phase flows, for configuration C1 using the "32Hz" tubes, instability does not arise in the tested reduced velocities up to this boundary. This is highlighted in Fig. 24 by enclosing the experimental data obtained at maximum reduced flow velocity (blue circles) and pointing to a putative higher value of the corresponding Connors "constant" K . Configuration C1 using the "14Hz" tubes became unstable in two-phase flows, leading to most values in the range $K = 6 \sim 10$.

These results are consistent with those obtained by Violette et al. (2006), as also shown in Fig. 24. As mentioned in the Introduction, the experimental results obtained by Nakamura and Tsujita (2018) for bundles with reduced pitch in the range $P/D=1.2\sim 1.5$ point to values $K = 7.5 \sim 10$, therefore are also consistent with our results. Concerning the experiments by Azuma et al. (2018), using SF6-Ethanol, with both straight bundles and U-bundles, they also observed streamwise instabilities in all cases. Interestingly, they obtained for the straight bundles the surprisingly low value $K \approx 2.5$, whereas for U-bundles they obtained values $K \geq 10$, depending on the tubes modal frequencies. Similar results seem to have been obtained by Nishida et al. (2021), in their steam-water experiments.

Recently, Panunzio et al. (2022) presented experimental results obtained using the same test rig as those of the present paper, but with the flexible tubes moving in the plane transverse to the flow direction. Their Connors stability map built from those single-phase and two-phase flow experiments, compared with the stability map of Fig. 24 pertaining to the in-flow experiments. Interestingly, the lower stability bound for the transverse motion (except for some data pertaining to the single flexible tube) is only marginally smaller than the lower stability bound for the in-flow motion. However, it would be risky to apply this conclusion to the upper stability bounds, as all the in-flow stability data pertaining to the two-phase flow configuration C1 with "32Hz" tubes is actually higher than plotted in Fig. 24. And, as discussed earlier, how much higher is actually unknown.

8. Conclusions

In this paper we presented experimental results for a rotated triangular straight tube bundle with reduced pitch $P/D=1.44$, providing new in-flow fluidelastic data for both single-phase (air or water) and two-phase (with homogeneous void fraction in the range 40% to 98%) transverse flows. Many different flexibility configurations were tested, with up to 15 flexible tubes, mounted with anisotropic supports allowing for in-flow vibrations. For the single-phase experiments, extensive modal identification of the flow-coupled tube bundle was performed under unmeasured turbulence excitation. The identification results obtained are consistent with finite element computations under stagnant flow. Moreover, they helped to disclose interesting changes concerning the unstable mode(s) as the flow velocity was increased beyond the linear stability boundary.

A conclusion from the ensemble of our tests, consistent with the main bulk of a (still limited) literature, is that streamwise instabilities may arise for $K \geq 6$, and often $K \geq 10$. However, this contrasts with the low values $K = 2.5 \sim 3.5$ obtained by Azuma et al. (2018) and Nishida et al. (2021) for some straight tube bundles (although not excited by the usual air-water flow mixture). Even so, Nishida et al. (2021) point that, for tubes with the same modal frequencies in the streamwise and transverse directions, the critical flow velocity for the transverse direction is lower than for the streamwise direction. These results clearly suggest that in-flow coupling forces are significantly smaller than those leading to out-of-plane instabilities. Actually, the topology of flows inside the bundles seem to support such idea.

All tested configurations with 2 to 7 in-line flexible tubes that became unstable did so when subjected to air flow, but not under water flow nor two-phase flow. The reason of such behavior is still unclear, but several lines of thought may be explored: (1) The denser fluids typically generate more damping, and this is particularly so concerning two-phase flows; (2) The denser flows further drift the flexible tubes from their nominal positions, and this may affect the destabilizing coupling forces; (3) The denser flows generate more effective random excitations and hence vibration amplitude, which might "break" the flow-coupling deterministic organization.

From the many experiments presented here, stems the important general conclusion that streamwise instability occurs only through the vibration coupling of *two or more tubes along the bundle columns*. This is a necessary condition, suggesting that streamwise instability cannot be theorized from a single-degree-of-freedom model. At least a model with two adjacent tubes of the same bundle column is needed, pointing to the significance of cross-coupling force terms. A somewhat similar

view was expressed by Nishida et al. (2021), when stating that a stiffness mechanism is dominant for streamwise instability.

Finally, we note that the lower stability bound for the flexible tubes transverse motion is only marginally smaller than the lower stability bound for the in-flow motion.

Acknowledgements

This work was performed in the framework of a joint research program co-funded by CEA, EDF and FRAMATOME (France). Valuable contributions by M. Bellanger and T. Valin (CEA-Saclay) to the experimental work are gladly acknowledged.

References

- Azuma, S., Morita, H., Hirota, K., Kondo, Y., Utsumi, S., Komuro, Y., Kawakami, R., Nariai, T., Nishikawa, Y. 2018. Investigation of critical flow velocity of a triangular U-tube bundle subjected to two-phase flow (Paper FIV2018-148). 9th International Symposium on Fluid-Structure Interactions, Flow-Sound Interactions, Flow-Induced Vibration and Noise, July 8-11, 2018, Toronto, Canada.
- CEA, 2022. Cast3m (finite element code). <http://www-cast3m.cea.fr/>
- Chen, S.S. 1983. Instability mechanisms and stability criteria of a group of circular cylinders subjected to cross-flow - Part 1: Theory. ASME Journal of Vibration, Acoustics, Stress and Reliability in Design 105, 52-58.
- Delaune, X. 2016. Literature review on the in-plane instability of steam generator tube bundles. CEA Internal Report (in French).
- Delaune, X., Piteau, P., Borsoi, L., Antunes, J. 2018. Experimental investigation of in-flow fluidelastic instability for square tube bundles subjected to single-phase and two-phase transverse flows (Paper FIV2018-49). 9th International Symposium on Fluid-Structure Interactions, Flow-Sound Interactions, Flow-Induced Vibration and Noise, July 8-11, 2018, Toronto, Canada.
- Feenstra, P., Sawadogo, T., Smith, B., Janzen, V., Cothron H. 2017. Investigations of in-plane fluidelastic instability in a multi-span U-bend tube bundle: Tests in air flow (Paper PVP2017-66068). ASME 2017 Pressure Vessels and Piping Conference, July 16-20, 2017, Waikoloa, Hawaii, USA.
- James, G.H. 1993. The natural excitation technique for modal parameter extraction from operating wing turbines. Report Nr. SAND92-1666, UC-261, Sandia National Laboratories, Albuquerque, USA.
- Janzen, V., Hagberg, E., Pettigrew, M., Taylor, C. 2005. Fluidelastic instability and work rate measurements of steam generator U-tubes in air-water cross-flow. ASME Journal of Pressure Vessel Technology 127, 84-91.
- Juang, J.N., Pappa, R. 1985. An eigensystem realization algorithm for modal parameter identification and model reduction. Journal of Guidance, Control Dynamics 8, 620-627.
- Kordkheili, S.A.H., Massouleh, S.H.M., Hajirezayi, S., Bahai, H. 2018. Experimental identification of closely spaced modes using NExT-ERA. Journal of Sound and Vibration 412, 116-129.
- Mureithi, N., Zhang, C., Ruël, M., Pettigrew, M. 2005. Fluidelastic instability tests on an array of tubes preferentially flexible in the flow direction. Journal of Fluids and Structures 21, 75-87.
- Nakamura, T., Tsujita, T. 2018. Study on stream-wise fluidelastic instability by air cross flow: Rotated triangular arrays inclined to flow (Paper FIV2018-19). 9th International Symposium on Fluid-Structure Interactions, Flow-Sound Interactions, Flow-Induced Vibration and Noise, July 8-11, 2018, Toronto, Canada.
- Nishida, S., Azuma, S., Morita, H., Hirota, K., Kawakami, R., Nishikawa, Y. 2021. In-plane fluidelastic instability evaluation of triangular array tube bundle using fluid force measured under steam-water two-phase flow condition. ASME Journal of Pressure Vessel Technology 143, 1-12 (Paper 011404).
- Panunzio, D., Lagrange, R., Piteau, P., Delaune, X., Antunes, J. 2022. Experimental investigation of cross-flow fluidelastic instability for rotated triangular tube bundles subjected to single-phase and two-phase transverse flows. 12th International Conference on Fluid-Induced Vibration, July 5-8, 2022, Paris-Saclay, France.
- Pappa, R.S., Elliott, K.B. 1993. Consistent-mode indicator for the Eigensystem Realization Algorithm. Journal of Guidance, Control, and Dynamics 16(5), 852-858.
- Piteau, P., Delaune X., Panunzio, D., Lagrange, R., Antunes, J. 2022. Experimental investigation of in-flow fluidelastic instability for rotated triangular tube bundles subjected to single-phase and two-phase transverse flows. 12th International Conference on Fluid-Induced Vibration, July 5-8, 2022, Paris-Saclay, France.

SCE - Southern California Edison, 2012. San Onofre nuclear generating station - Unit 2 return to service report. Document ML12285A263, retrieved from https://www.nrc.gov/docs/ML1228/ML12285_A263.pdf.

Tan, T., Gao, L., Li, P., Ma, J., Jiang, T. 2018. Experimental study on fluidelastic instability of rotated triangular tube bundles subjected to two-phase cross flow (Paper FIV2018-64). 9th International Symposium on Fluid-Structure Interactions, Flow-Sound Interactions, Flow-Induced Vibration and Noise, July 8-11, 2018, Toronto, Canada.

Violette, R., Pettigrew, M., Mureithi, N. 2006. Fluidelastic instability of an array of tubes preferentially subjected to two-phase cross flow. *ASME Journal of Pressure Vessel Technology* 128, 148-159.

Weaver, D., Koroyannakis, D. 1983. Flow-induced vibrations of heat exchanger U-tubes: A simulation to study the effects of asymmetric stiffness. *ASME Journal of Vibration, Acoustics, Stress and Reliability in Design* 105, 67-75.

Weaver, D., Schneider, W. 1983. The effect of flat bar supports on the crossflow induced response of heat exchanger U-tubes. *ASME Journal of Engineering for Power* 105, 775-78.